scientific reports

OPEN

Human cerebral spheroids undergo 4-aminopyridine-induced, activity associated changes in cellular composition and microrna expression

Thomas Parmentier[1,6], Fiona M. K. James[2], Elizabeth Hewitson[1], Craig Bailey[1], Nicholas Werry[1], Steven D. Sheridan[3,4], Roy H. Perlis[3,4], Melissa L. Perreault[1], Luis Gaitero[2], Jasmin Lalonde[5] & Jonathan LaMarre[1✉]

Activity-induced neurogenesis has been extensively studied in rodents but the lack of ante mortem accessibility to human brain at the cellular and molecular levels limits studies of the process in humans. Using cerebral spheroids derived from human induced pluripotent stem cells (iPSCs), we investigated the effects of 4-aminopyridine (4AP) on neuronal activity and associated neurogenesis. Our studies demonstrate that 4AP increases neuronal activity in 3-month-old cerebral spheroids while increasing numbers of new neurons and decreasing the population of new glial cells. We also observed a significant decrease in the expression of miR-135a, which has previously been shown to be decreased in exercise-induced neurogenesis. Predicted targets of miR-135a include key participants in the SMAD2/3 and BDNF pathways. Together, our results suggest that iPSC-derived cerebral spheroids are an attractive model to study several aspects of activity-induced neurogenesis.

Human brain development is a highly orchestrated process during which precursors of neuronal and glial cells organize, as they differentiate, into specialized cellular circuits required for normal function. Because neurogenesis and gliogenesis in humans occur primarily in utero, studying these processes, and understanding how they may contribute to the onset and progression of certain neurological disorders, is particularly challenging. The discovery that neurogenesis continues in certain discreet regions of the adult brain, in particular the dentate gyrus of the hippocampus, has improved our knowledge of the factors that modulate neurogenesis and the functional implications of adding new neurons to existing neuronal networks[1–3]. Interestingly, postnatal hippocampal neurogenesis is enhanced by different stimuli that increase activity, such as hippocampal-dependent learning tasks, long-term potentiation, exposure to an enriched environment, and motor activity[4–6]. Epileptic seizures, which are uncontrolled events where the brain undergoes a pathological increase in neuronal activity, have also been found to increase the formation of new neurons[7]. This activity-dependent postnatal neurogenesis phenomenon is attributed to both an increase in proliferation and differentiation of neural stem cells and an increase in the survival of newly formed neurons[3,4].

The molecular underpinnings of activity-dependent neurogenesis, and how they relate to human brain development in utero, are not well understood. Neural stem cells have been shown to respond to neurotransmitters and growth factors released by neurons which then can influence the proliferation and differentiation of these neural stem cells both in vitro and in vivo[8–11]. Because of inherent limits in probing the developing human brain, and the scarcity of human fetal brain samples, the cellular and molecular mechanisms of activity-dependent neurogenesis as well as the scope of this process in human brain development are not well known. Recently,

[1]Department of Biomedical Sciences, Ontario Veterinary College, University of Guelph, Guelph, ON, Canada. [2]Department of Clinical Studies, Ontario Veterinary College, University of Guelph, Guelph, ON, Canada. [3]Center for Quantitative Health, Center for Genomic Medicine and Department of Psychiatry, Massachusetts General Hospital, Boston, MA, USA. [4]Department of Psychiatry, Harvard Medical School, Boston, MA, USA. [5]Department of Molecular and Cellular Biology, College of Biological Science, University of Guelph, Guelph, ON, Canada. [6]Present address: Département de Sciences Cliniques, Faculté de Médecine Vétérinaire, Université de Montréal, Montréal, QC, Canada. ✉email: jlamarre@uoguelph.ca

cerebral organoids, a new model of human brain development has been described using human pluripotent stem cells and was shown to recapitulate key milestones of human brain development[12–15]. Cerebral organoids contain most of the diversity of cell types that are present in the developing human brain and self-organize similarly in this model[15–18]. Moreover, with increasing time in culture, cerebral organoids generate complex oscillatory activity that cannot be recapitulated with more simple culture methods such as neurospheres that are 3D aggregates lacking the layered organization of cerebral organoids[19]. Given their ability to capture many key features of human brain development, cerebral organoids have recently been used to model several neurodevelopmental disorders in vitro and study the effect of impaired neurogenesis on neuronal network activity[20–22]. However, it is unknown whether activity-induced neurogenesis can be recapitulated in human cerebral organoids. In this study, we explore the effects of 4-aminopyridine (4AP)—an organic compound known to increase neuronal activity in ex vivo brain slices—on the neuronal activity in cerebral organoid and its global effect on neurogenesis. In addition, we examine the changes in specific microRNAs (miRNAs) that are associated with neurogenesis in vivo. Overall, our study provides a platform for the investigation of activity-dependent neurogenesis in a complex model of human brain development.

Results

Recapitulation of neurogenesis and gliogenesis in cerebral spheroids.
Different protocols have been used to generate cerebral organoids from human pluripotent stem cells. To help ensure consistency in cerebral organoid generation in between cell lines and batches, we used a guided protocol that was designed to result in neurons demonstrating a cortical phenotype. This protocol has been shown to reliably generate cerebral organoids termed "cortical spheroids" by dual SMAD inhibition to direct pluripotent stem cells to a neuroectodermal phenotype and then neurons with a dorsal forebrain identity[23]. We first verified the development of spheroids by employing immunofluorescence identification of cell types using three different iPSC lines derived from neurologically normal individuals. Embryoid bodies were successfully generated from all 3 iPSC lines and the resulting spheroids progressively increased in size during culture (Supplemental Fig. 1). Upon dual SMAD inhibition, cells expressed the neuroectodermal cell marker SOX2 and organized into polarized neural tube-like structures (Fig. 1a). Neural progenitor cells expressing the marker Nestin and proliferative marker Ki67 were present in these neural tube-like structures and were radially organized (Fig. 1b–d). Neural progenitor cells progressively differentiated into neuroblasts expressing the marker DCX as well as post-mitotic neurons expressing MAP2 and NeuN localized at the periphery of the neural tube-like structures. Glial cells expressing GFAP appeared around day 60 and progressively increased in number (Fig. 1d,e). This pattern of differentiation with progressive emergence of neuroblasts, post-mitotic neurons and then glial cells is consistent with what has been described in other studies[19,24].

To verify that putative neurons within the organoids also acquired relevant functional properties, we performed whole-cell recordings of putative neurons in cerebral spheroids between maturation days 70–80 and days 115–120. Functional neuronal maturation was observed through an increase in action potential amplitude, a decrease in membrane resistance and a trend towards an increase in rheobase as neurons matured (Table 1). Spontaneous action potentials and putative spontaneous excitatory post-synaptic potentials (sEPSCs) were observed (Fig. 2a). Furthermore, all excitable cells that were subjected to recording between days 70–80 developed a depolarization block when injected 100 pA (3/3) whereas only 2/8 excitable cells developed a depolarization block after the same stimulation at day 115–120 (Fig. 2b–d). Unfortunately, the whole-cell recording procedure proved particularly challenging under these circumstances with 3/11 and 8/21 cells that were successfully acquired were excitable at days 70–80 and 115–120 respectively (Table 1). This relatively low success rate may be attributable to low cell survival after the slicing procedure, immaturity of the neurons in spheroids at these time points and the technical difficulty of whole-cell electrophysiology. Nevertheless, several neurons with mature electrophysiological properties were consistently acquired and recorded, confirming the reliability of the chosen protocol.

Effect of 4AP on neuronal excitability in cerebral spheroids.
To investigate whether we could increase neuronal activity in 90-day old cerebral spheroids, we incubated them with 4AP which has been shown to increase neuronal activity in brain slices and to induce epileptic seizures in vivo[25–27]. We first followed neuronal activity in individual cells with fluorescent calcium imaging. As expected, 4AP treatment resulted in an approximately four-fold increase in the number of active cells (67.1956% vs 17.2247%) and in the frequency of calcium waves (71.7704 mHz vs 16.1405 mHz) in active cells of spheroids (Fig. 3a–c). Calcium waves had larger mean amplitudes but shorter mean durations in cells of 4AP-treated spheroids compared to controls (Fig. 3d,e). To assess neuronal activity with higher temporal resolution and evaluate synchronization within spheroids, we placed individual 90-day old spheroids directly on multi-electrode arrays (MEA). MEA recordings also showed increases in the mean spike firing rate after exposure to 4AP, although it did not reach statistical significance, likely due to variability in the firing rate between individual spheroids (Fig. 3f,g). In addition, spheroids demonstrated bursts of activity after exposure to 4AP, which were not observed prior to exposure (electrode burst average frequency 19.3 mHz). These bursts had an average duration of 199 ms ± 2 ms (Fig. 3h). However, neuronal activity remained unsynchronized even after stimulation with 4AP (mean synchrony index: 0.0040 and 0.0126 before and after 4AP exposure respectively). To verify whether 4AP activated in neurons within spheroids, we evaluated the proportion of postmitotic NeuN + neurons that expressed the immediate early gene cFos in organoids exposed to 4AP compared to controls. These NeuN +/cFos + neurons represent putative recently stimulated neurons. As expected, the proportion of NeuN +/cFos + double-positive neurons was higher in spheroids exposed to 4AP than control spheroids (51.1% vs 15.5% respectively; Fig. 3i,j). This result demonstrates that 4AP
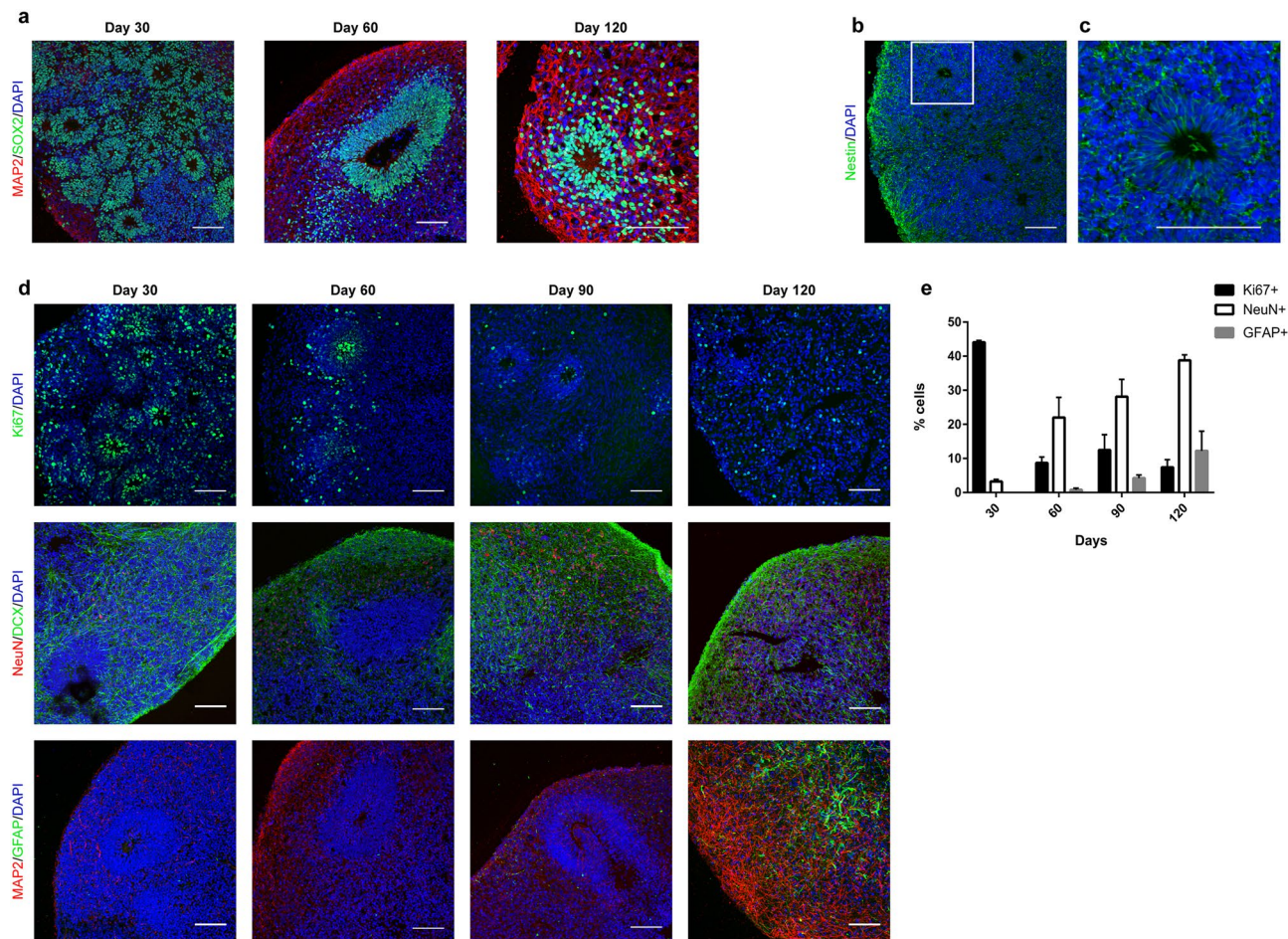
Figure 1. Neurogenesis and gliogenesis in cerebral spheroids. (**a**) Representative immunofluorescence images of cerebral spheroids stained for neuroectodermal cell (SOX2) and post-mitotic neuron (MAP2) markers after 30, 60 or 120 days of culture. Bars = 100 μm. (**b**) NSCs express the neural stem cell marker Nestin. A spheroid at day 30. Bar = 100 μm. (**c**) Enlargement of white square in (**b**) showing that Nestin-positive NSCs are radially organized in a neuroepithelium-like structure. Bar = 100 μm. (**d**) Representative immunofluorescence images of cerebral spheroids stained for neuroectodermal proliferative cell (Ki67), immature neuron (DCX), post-mitotic neuron (MAP2, NeuN) or glial cell (GFAP) markers after 30, 60, 90 and 120 days of culture. Bars = 100 μm. (**e**) Quantification of cells expressing specific markers for proliferation (Ki67), neurogenesis (NeuN) and gliogenesis (GFAP). Data represent mean ± SEM of 2–3 organoids/cell line, 3 different iPSC lines.

Time in culture (days)	Number excitable cells/ number recorded cells	Resting membrane potential (mV) Mean ± (SEM)	Membrane resistance (MΩ) Mean ± (SEM)	Spike amplitude (mV) Mean ± (SEM)	Rheobase (pA) Mean ± (SEM)	sEPSCs amplitude (pA) Mean ± (SEM)
70–80	3/11	− 53.33 ± 12.13	1367 ± 145.3	32.94 ± 11.09	8.333 ± 3.333	− 20.47 ± 0.4487
115–120	8/21	− 59.75 ± 3.138 (p = 0.4719)	850.5 ± 104 (p = 0.0255)	59.75 ± 2.28 (p = 0.0211)	19.38 ± 2.903 (p = 0.0642)	− 22.12 ± 2.905 (p = 0.4970)

Table 1. Electrophysiological properties of patched cells across time in culture. Summary of electrophysiological characteristics of excitable cells in cerebral spheroids recorded with whole-cell recordings. Student's *t*-test.

increased neuronal activity and induced a higher expression of the IEG cFOS in post-mitotic neurons. Overall, 4AP increased neuronal activity in 90-day-old cerebral spheroids.

We verified that cerebral spheroids could form mature neuronal networks with synchronization by repeating the MEA recordings on 160-day-old spheroids (Fig. 4a). Interestingly, while network bursts were not observed in unstimulated 160-day-old spheroids, exposure to 4AP triggered the appearance of synchronized network bursts in 3/4 spheroids with a frequency of 109.9 ± 4.9 mHz (Fig. 4a). These network bursts had a duration of 1.5 ± 0.4 s and during the bursts, spike frequency was 611.9 Hz ± 217.8 Hz. Although we observed an increase in mean firing rate (Fig. 4b), electrode burst rate (Fig. 4c) and network burst rate (Fig. 4d) in spheroids exposed to 4AP compared to control, high variability was observed within spheroids and the differences did not reach
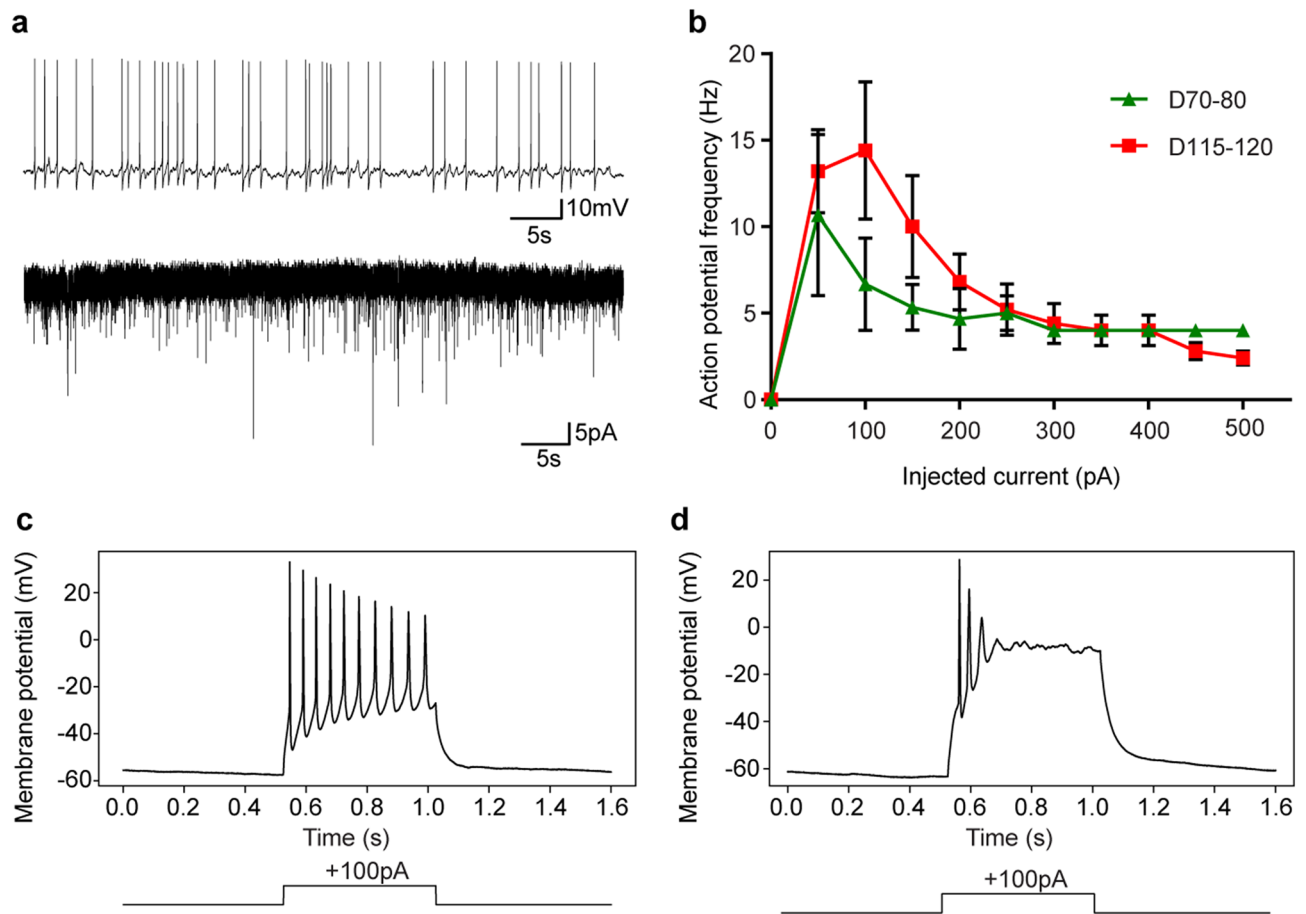
Figure 2. Electrophysiological properties of neurons in cerebral spheroids. (**a**) Upper trace: representative trace in current clamp mode showing spontaneous action potentials. Lower trace: representative trace in voltage-clamp mode showing spontaneous putative sEPSCs. (**b**) Input–output curves as a measure of excitability in spheroids at different times of culture. Neurons in spheroids show a maximum action potential frequency around 50–100 pA of injected current after which a depolarization block is observed. Data represents mean ± SEM of excitable cells described in Table 1. No statistical difference observed between day 70–80 and day 115–120. (**c**) Example of a burst of action potentials in a putative mature neuron triggered by 100 pA of injected current. (**d**) Example of a depolarization block in a putative immature neuron.

statistical significance. Compared to 90-day-old spheroids, 4AP increased synchronization of activity in 160-day-old spheroids by approximately 12-fold without reaching statistical significance (synchrony index: 0.0062 vs 0.0755 before and after 4AP exposure respectively, Fig. 4e).

These findings reveal that synchronized network bursts could be triggered in cerebral spheroids with 4AP after 160 days of culture. This suggests that while 4AP increases neuronal activity in 90-day-old spheroids, these spheroids require a longer time in culture to generate synchronized activity.

4-aminopyridine-induced neurogenesis in cortical spheroids. Activity-induced neurogenesis has been documented both in vitro and in vivo. We next examined whether neurogenesis was similarly modulated in spheroids by 4AP-induced changes in neuronal activity. We evaluated neurogenesis in 90-day-old spheroids as a significant number of SOX2 + neural stem cells are still present and organized in neural tube-like structures at that stage compared to older spheroids. First, we analyzed the effect of 4AP on proliferation and noted an approximately twofold decrease in the number of proliferative Ki67-positive cells after 24 h of 4AP exposure (2.2963% vs 4.367%, Fig. 5a). We next identified a small but not statistically significant increase in apoptotic cleaved-caspase3-positive cells in 4AP treated organoids (0.1875% vs 0.3019%, Fig. 5b).

We then investigated whether 4AP affected the differentiation of NSCs by tagging proliferating cells with EdU just prior to stimulation with 4AP and assessing their differentiation 2 weeks later using antibodies against immature neurons (DCX), mature neurons (NeuN) or glial cells (GFAP). No statistically significant difference was found in the proportion of EdU + /DCX + cells between 4AP-treated and control spheroids (47.4% vs 58.3% respectively, Fig. 5c). In contrast, a higher proportion EdU-positive cells in 4AP-treated spheroids expressed the mature neuron marker NeuN compared to control spheroids (20.6% vs 11.6% respectively, Fig. 5d). We also observed a higher proportion of EdU-positive cells expressed the glial cell marker GFAP in control spheroids compared to 4AP-treated spheroids (28.2% vs 13.6% respectively, Fig. 5e). Overall, this suggests that proliferating
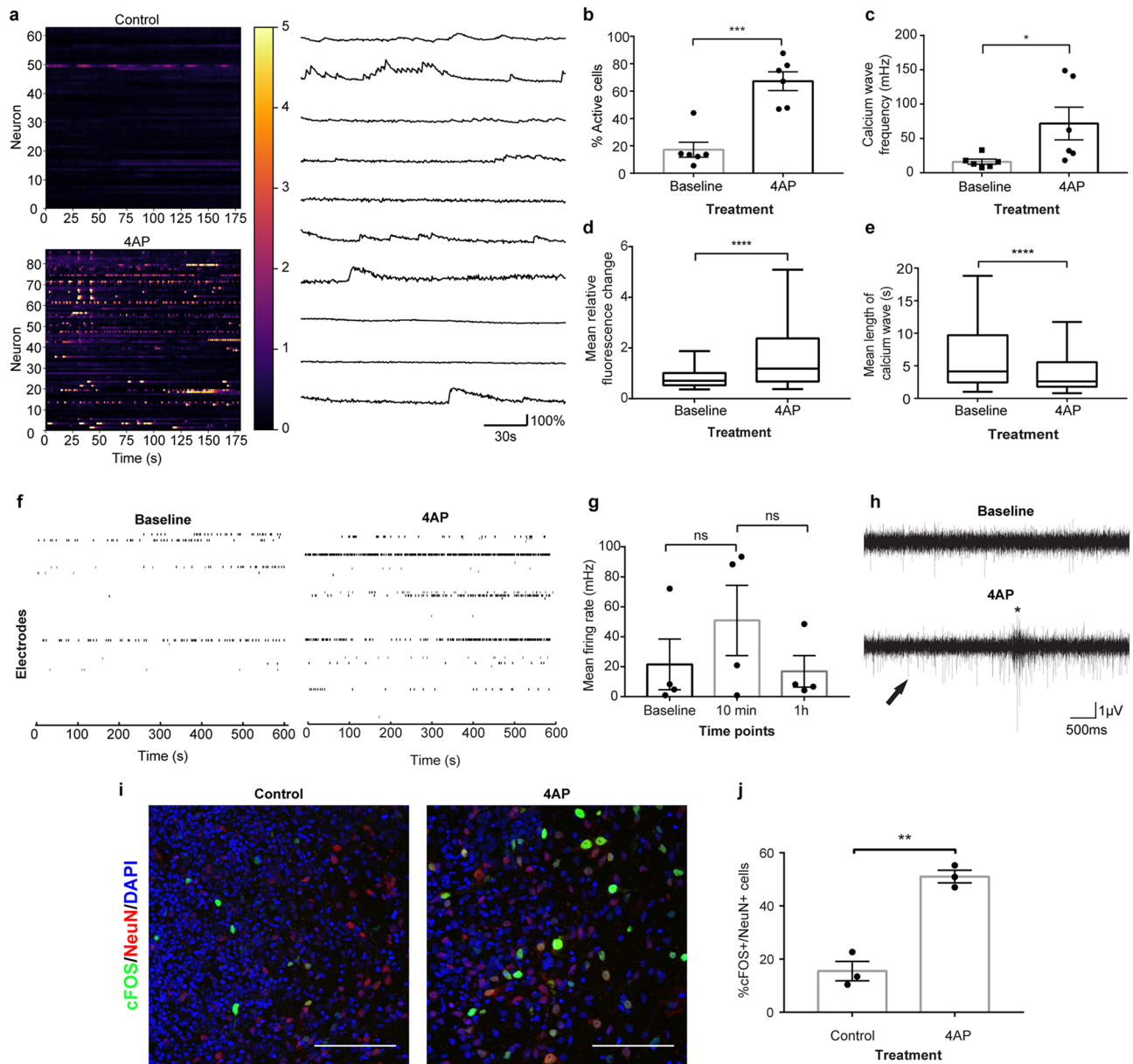
Figure 3. Effect of 4AP on neuronal activity in 90-day-old cerebral spheroids. (**a**) Left: Heatmap of calcium-associated fluorescence over time in a spheroid before exposure to 4AP (upper) and after exposure to 4AP (lower). Each line represents a different cell and the color bar represents the fold-change in calcium-associated fluorescence over each cell's baseline. Right: Individual traces of calcium-associated fluorescence over time of representative cells (**b**) Proportion of active cells before and after treatment with 4AP. Student's t-test, $p = 0.0003$. Bars represent mean ± SEM. Each dot represents an individual spheroid, n = 6 spheroids/condition *** $p < 0.001$. (**c**) Calcium wave frequency in active cells exposed or not to 4AP. Wilcoxon Rank Sum test, $p = 0.0152$. Bars represent mean ± SEM. Each dot represents an individual spheroid, n = 6 spheroids/condition * $p < 0.05$. (**d**) Mean calcium transient amplitude. The mean calcium transient amplitude was calculated for each cell from 6 individual spheroids for each condition (n = 282 cells in 4AP group and 95 cells in Baseline group. Wilcoxon Rank Sum test, $p < 0.0001$. The line represents the median, sides of the box represent the upper and lower quartile and whiskers represent maximum and minimum values. **** $p < 0.0001$. (**e**) Mean calcium transient duration. The mean calcium transient duration was calculated for each cell from 6 individual spheroids for each condition (n = 282 cells in 4AP group and 95 cells in Baseline group. Wilcoxon Rank Sum test, $p < 0.0001$. The line represents the median, sides of the box represent the upper and lower quartile and whiskers represent maximum and minimum values. **** $p < 0.0001$. (**f**) Representative raster plot of neuronal spikes before (left) and after (right) exposure to 100 μM 4AP. Each line represents an individual electrode. (**g**) Mean firing rate upon exposure to 4AP. ANOVA repeated measures with Holm Sidak's correction for multiple comparisons, $F_{(1,439,4,316)} = 0.6389$ $p = 0.5226$. Each dot represents an individual spheroid, n = 4 spheroids/condition. Bars represent mean ± SEM. ns: not significant. (**h**) Example traces of local field potentials recorded before (upper) and after (lower) 10-min exposure to 4AP showing an increase in spikes (arrow) as well as the presence of bursts (*). (**i**) Representative immunofluorescence image of cFOS + /NeuN + recently active neurons in spheroids exposed to vehicle (left) or 4AP (right). Bar = 100 μm. (**j**) Proportion of cFOS + /NeuN + in NeuN + neurons in spheroids exposed or not to 4AP. Student's t-test, p = 0.0034. Bars represent mean ± SEM. Each dot represents an individual spheroid. **p < 0.01.
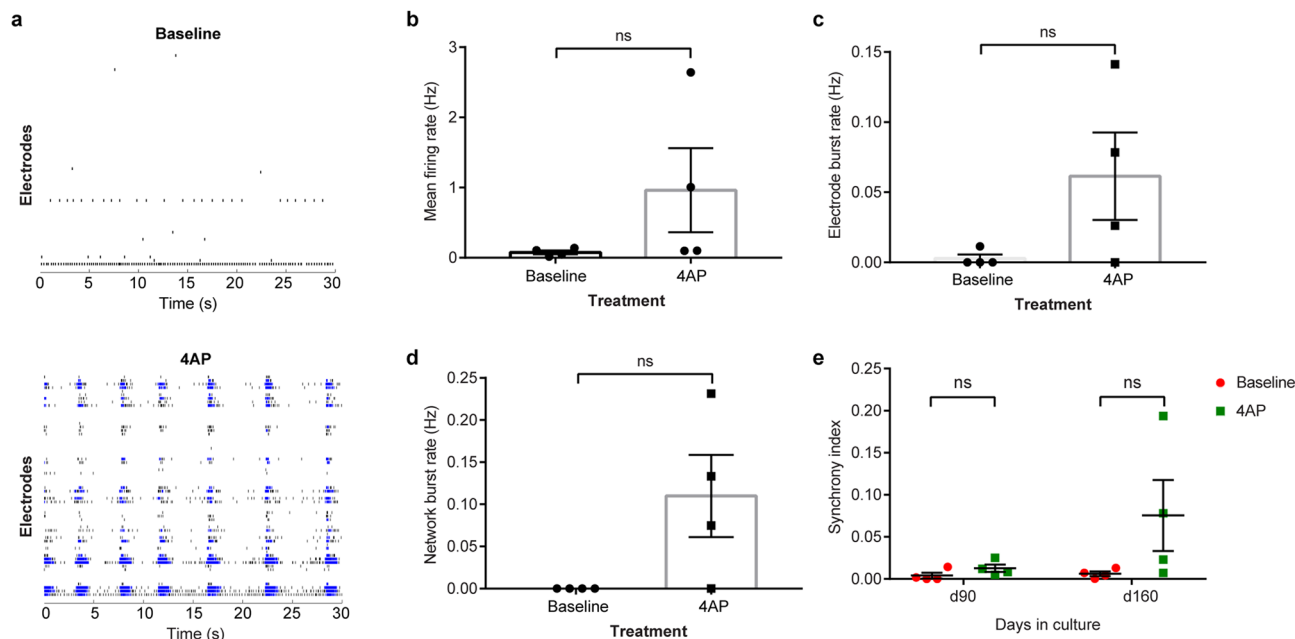
Figure 4. Effect of 4AP on neuronal activity in 160-day-old cerebral spheroids. (**a**) Representative raster plots of a 160-day-old cerebral spheroids before (upper) and after exposure (lower) to 4AP. Exposure to 4AP triggered network bursts characterized by synchronous bursting of several electrodes. Black marks indicate individual spikes while blue marks indicate electrode bursts. (**b**) Mean firing rate in spheroids before and after exposure to 4AP. Paired Student's t-test, $p = 0.2327$. Bars represent mean ± SEM. Each dot represents an individual spheroid, n = 4 spheroids/condition ns: not significant. (**c**) Electrode burst frequency in spheroids before and after exposure to 4AP. Paired Student's t-test, $p = 0.1750$. Bars represent mean ± SEM. Each dot represents an individual spheroid, n = 4 spheroids/condition. ns: not significant. (**d**) Network burst frequency in spheroids before and after exposure to 4AP. Paired Student's t-test, $p = 0.1097$. Bars represent mean ± SEM. Each dot represents an individual spheroid, n = 4 spheroids/condition. ns: not significant. (**e**) Synchrony index before and after exposure to 4AP at day 90 and day 160. Paired Student's t-test, $p_{day\ 90} = 0.1762$ and $p_{day\ 160} = 0.1528$. Bars represent mean ± SEM. Each dot represents an individual spheroid, n = 4 spheroids/condition. ns: not significant.

cells at the time of 4AP exposure are more likely to differentiate into neurons and less into glial cells under these conditions.

4-aminopyridine-induced changes in microRNA expression in spheroids. MicroRNAs are involved in the regulation of gene expression and implicated in neuronal differentiation of NSCs[28,29]. Moreover, the expression of specific miRNAs is induced by neuronal activity[30]. We therefore hypothesized that, if certain miRNAs were implicated in activity-induced neurogenesis, we would observe differential expression of these miRNAs in spheroids treated with 4AP. We focused on 9 miRNAs previously demonstrated to participate in neurogenesis and consistently differentially expressed in rodent models of epilepsy as well as human epileptic tissue[31]. Of the 9 miRNAs selected, only miR-135a was differentially expressed between treated and control spheroids; its expression was significantly decreased in spheroids exposed to 4AP (Fold change: 0.72; Fig. 6a). The decrease in miR-135a expression after exposure to 4AP could be either due to decreased transcription or increased turnover. To investigate this further, we measured the expression of pri-miR-135a by RT-qPCR. MiR135a is encoded by two genes: *MIR135A1* on human chromosome 3 and *MIR135A2* on human chromosome 12. We designed primers specific for each stem-loop transcript (pri-miR-135a1, pri-miR-135a2) and measured the expression of each transcript using RT-qPCR. Interestingly, only pri-miR-135a2 showed a decrease in expression in the spheroids treated with 4AP (Fig. 6b). This suggests that the observed decrease in mature miR135a is due to at least in part to a decrease in transcription of the *MIR135A2* gene or increased turnover of pri-miR-135a2 prior to processing into its mature form.

The *MIR135A2* gene is located in the last intron of *RMST*, a gene coding for the long non-coding RNA RMST[32]. The transcription of intragenic miRNAs can be either under the control of promoters of the host gene in which they are located, or through nearby independent promoters. To begin to elucidate whether *MIR135A2* transcription is under the control of the *RMST* promoter in our spheroid model, we measured the expression of the RMST transcript in spheroids treated with 4AP and in control spheroids and observed a decrease in RMST expression in 4AP-treated spheroids (0.6-fold change; Fig. 6c). We then plotted the level of expression of pri-mir-135a2 and mir-135a as a function of the level of expression of RMST and observed a strong correlation between them ($r^2 = 0.8787$ and $r^2 = 0.8603$ respectively; Fig. 6d,e). Altogether, this suggests that the decrease in miR-135a
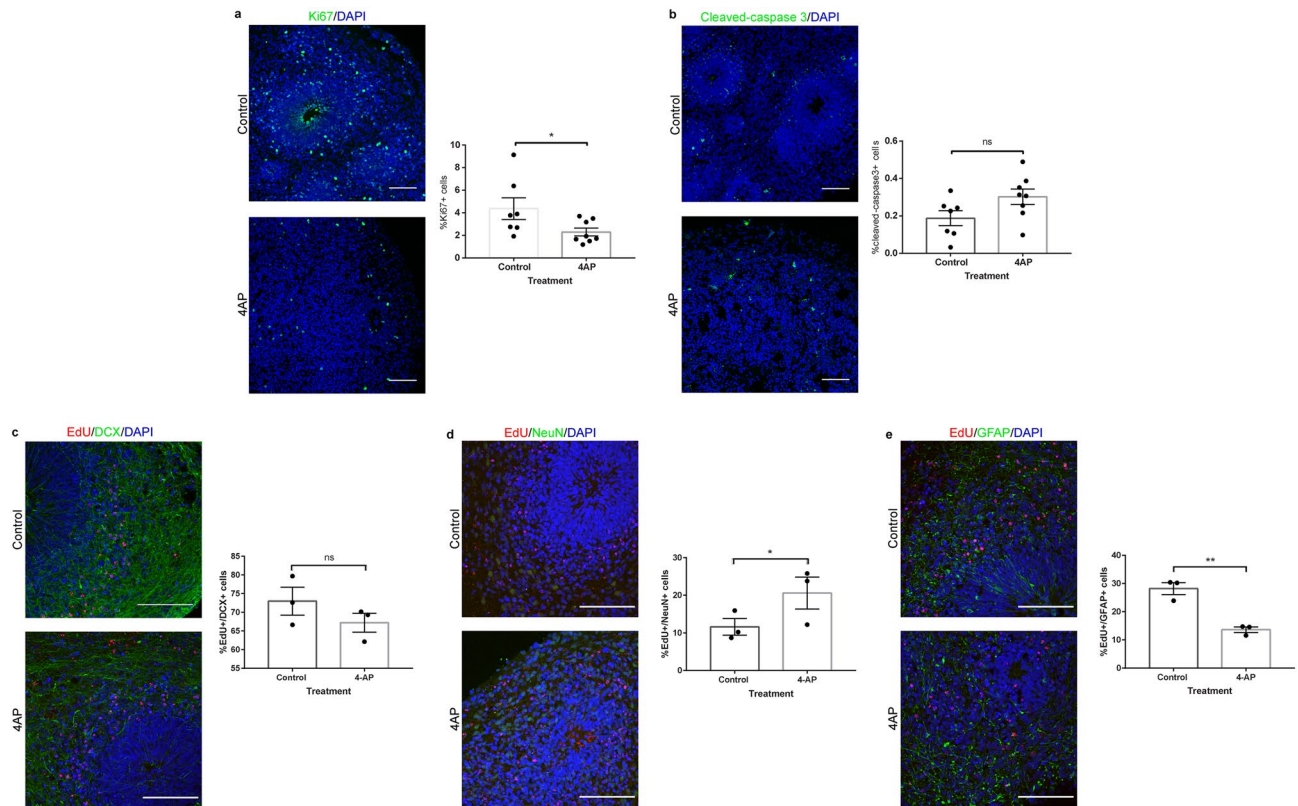
Figure 5. 4-aminopyridine-induced apoptosis, proliferation, neurogenesis and gliogenesis in cerebral spheroids. (**a**) Representative immunofluorescence image (left) and proportion of Ki67-positive proliferative cells (right) 24 h after treatment with 4AP or vehicle (water). Student's *t* test with Holm Sidak's correction for multiple comparisons, $p = 0.0331$. Bars represent mean ± SEM. Each dot represents an individual spheroid, n = 7 control spheroids and 8 treated spheroids. *$p < 0.05$. (**b**) Representative immunofluorescence image (left) and proportion of cleaved-caspase 3-positive apoptotic cells (right) 24 h after treatment with 4AP or vehicle (water). Student's *t* test with Holm Sidak's correction for multiple comparisons, $p = 0.0995$. Bars represent mean ± SEM. Each dot represents an individual spheroid, n = 7 control spheroids and 8 treated spheroids. ns: not significant. (**c**) Representative immunofluorescence image (left) and proportion of EdU + /DCX + cells in EdU + cells. Student's *t* test with Holm Sidak's correction for multiple comparisons, $p = 0.0880$. Bars represent mean ± SEM. Each dot represents an individual spheroid, n = 3 spheroids/condition. ns: not significant. (**d**) Representative immunofluorescence image (left) and proportion of EdU + /NeuN + cells in EdU + cells. Student's *t* test with Holm Sidak's correction for multiple comparisons, $p = 0.0331$. Bars represent mean ± SEM. Each dot represents an individual spheroid, n = 3 spheroids/condition. *$p < 0.05$. (**e**) Representative immunofluorescence image (left) and proportion of EdU + /GFAP + cells in EdU + cells. Student's *t* test with Holm Sidak's correction for multiple comparisons, $p = 0.0073$. Bars represent mean ± SEM. Each dot represents an individual spheroid, n = 3 spheroids/condition. **$p < 0.01$. Bars = 100 μm for all immunofluorescence images.

expression is due at least partly to a decrease in *RMST* transcription, although increased turn-over of the RMST primary transcript may also contribute to the decrease in pri-mir135a2 levels.

To identify the potential functional significance of miR-135a differential expression after 4AP treatment, we investigated the 512 mRNA targets of miR-135a reported by one or more databases of validated miRNA-mRNA interactions. These mRNA targets were subjected to GO and KEGG enrichment analysis to identify potential functional pathways. GO enrichment analysis for biological processes revealed a significant enrichment for terms related to negative regulation of biosynthetic processes and transcription. GO: molecular function terms were enriched for kinase binding as well as transcription factors and chromatin binding factors. GO: cellular components were enriched for neuronal components such as the synapse and dendrites. Finally, KEGG pathway terms were enriched for SMAD2/3 and BDNF signaling suggesting a role of miR-135a targets in growth and differentiation (Fig. 6f–i). This supports roles for miR-135a in activity-induced neurogenesis at least in part by targeting transcription factors that, once activated, drive NSCs toward the neuronal lineage.

Discussion
Here we present some of the first evidence to support 4AP-induced, activity associated changes in neurogenesis and concomitant changes in miRNA expression in cerebral spheroids. 4AP increased neuronal activity in 90-day-old spheroids although a longer time in culture was required for the appearance of synchronized activity. This is in line with a previous study that has reported little synchronization in 2–4 months old organoids but a gradual
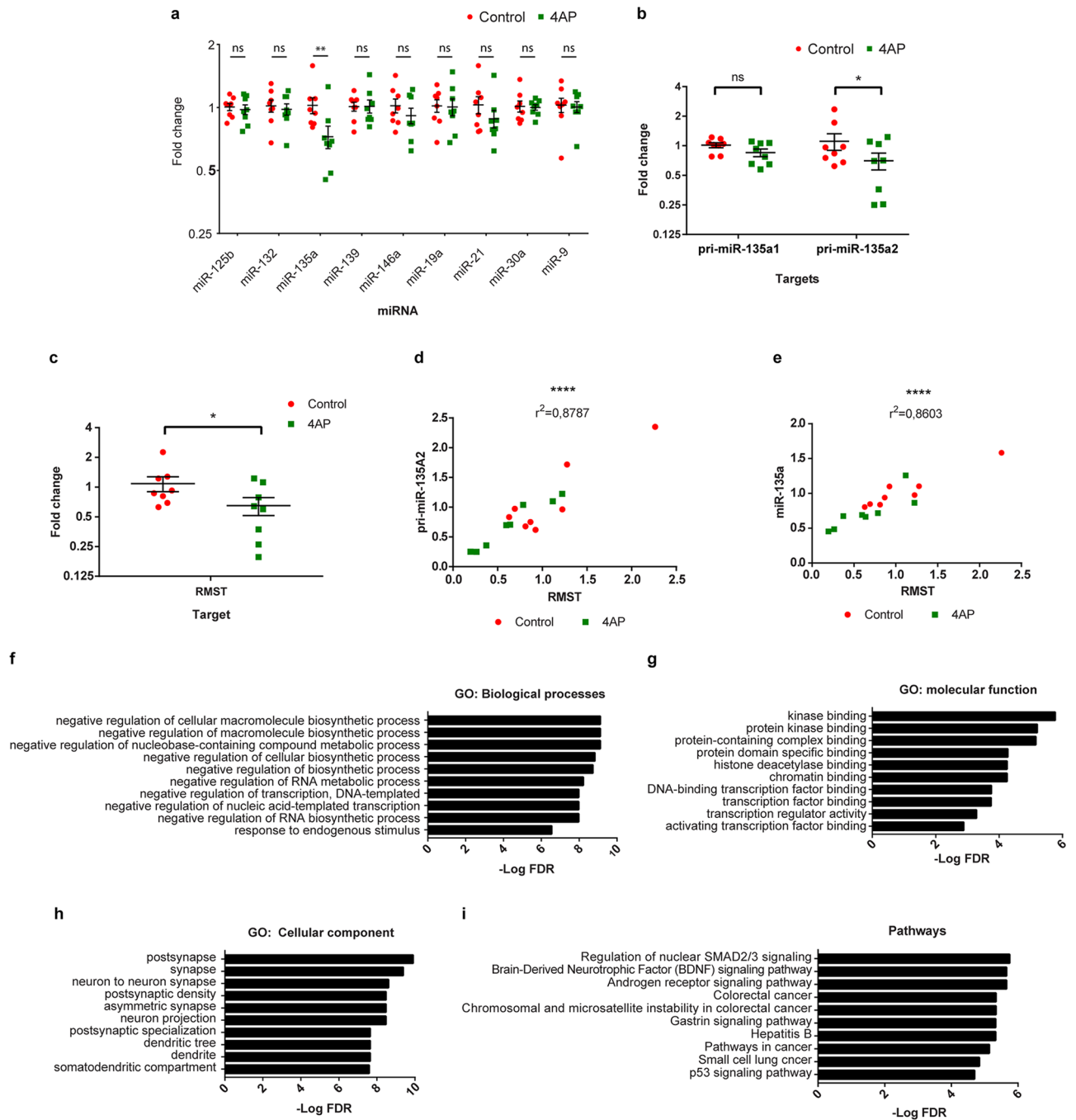
Figure 6. 4-aminopyridine-induced expression of cFOS, epilepsy-associated miRNAs and RMST in cerebral spheroids. (**a**) Expression of epilepsy-associated miRNAs in spheroids. ANOVA followed by multiple Student's t test with Holm Sidak's test for multiple comparisons. $F_{(1, 126)} = 5.63$, $p = 0.0192$, $p_{miR-135a} = 0.0053$. Bars represent mean ± SEM. Each dot represents an individual spheroid, $n = 8$ spheroids in each group. ns: not significant, **$p < 0.01$. (**b**) Expression of pri-mir-135a1 and pri-mir-135a2 in cerebral spheroids exposed to 4AP or not. Expression was measured with RT-qPCR. ANOVA followed by multiple Student's t-test with Holm Sidak's test for multiple comparisons. $F_{(1, 28)} = 5.401$, $p = 0.0276$, $p_{pri-miR-135a2} = 0.046$, $p_{pri-miR-135a1} = 0.385$. Bars represent mean ± SEM. Each dot represents an individual spheroid, $n = 8$ spheroids in each group ns: not significant, *$p < 0.05$. (**c**) Expression of RMST in cerebral spheroids exposed to 4AP or not. Expression measured with RT-qPCR. Student's t-test, $p = 0.0453$. Bars represent mean ± SEM. Each dot represents an individual spheroid, $n = 8$ spheroids in each group. *$p < 0.05$. (**d**,**e**) Correlation between RMST expression and pri-mir-135A2 and miR-135a respectively. Pearson correlation coefficient. Each dot represents an individual spheroid, $n = 8$ spheroids in each group ****$p < 0.0001$. (**f–i**) Enrichment analysis for miR-135a targets. Top 10 terms for GO biological processes (**f**), GO molecular function (**g**), GO cellular components (**h**) and KEGG pathway (**i**). *FDR* False Discovery Rate.

increase in neuronal spontaneous depolarization events until 8 months of culture[19]. Although our electrophysiological data is not definitive with regard to the effects of 4-aminopyridine on neuronal activity, our calcium imaging data strongly support an increase in neuronal activity due to 4-aminopyridine exposure. Calcium imaging has been used as a valid proxy for neuronal activity by many groups in other important studies[33–36]. Potential drawbacks of calcium imaging performed on intact spheroids are that the calcium indicator may not penetrate in cells deeper in the spheroids, may not identify cells outside the focal plane of the microscope, may not demonstrate high temporal resolution, and may not identify some changes in cellular membrane potential. However, when cellular calcium fluxes of the type reported here are observed, they are strongly associated with neuronal activity and membrane depolarization[33–36]. In the present study we attempted to support our calcium imaging observations by employing MEA recording using a previously described protocol[19]. However, this technique was challenging and provided limited data as spheroids repeatedly detached from the MEA plate, preventing recording. We therefore modified the technique and placed the organoids on the plate for a more limited period to allow transient attachment to the recording array. This method has been successfully employed for organoids other studies[37–39]. Although this approach allowed us to satisfactorily record from the intact organoid, rather than outgrowth cells present in longer-maintained cultures, fewer active electrodes were engaged, which may have contributed to the low efficiency and higher variability observed in our recordings. Future studies in which the adhesion of the spheroids to electrodes is improved through coating with poly-ornithine, laminin or polyethyleneimine or physically enforced with a harp slice grid placed over the spheroids to submerge it completely[19,40,41] will likely be necessary to resolve this issue.

The increase in newly formed neurons (EdU + /NeuN +) and decrease in newly formed glial cells (EdU + / GFAP +) in spheroids treated with 4AP constitutes striking evidence for 4AP-induced neurogenesis in spheroids. Of note, similar evidence highlighting the effect of neuronal activity on neuronal and glial differentiation has been described both in vitro and in vivo[10,11,42,43]. However, we did not determine whether the increase in neuronal differentiation observed in spheroids is mediated directly through the increase in neuronal activity by 4AP or through an independent action of 4AP on NSCs. 4AP blocks potassium channels leading to an increase in neurotransmitter release in pre-synaptic neurons and inhibits repolarization in post-synaptic neurons, but other effects notably on NSCs have not been studied[44]. NSCs exhibit outward potassium currents and blockade of these currents affect the proliferation of viability of NSCs. Importantly for our study, these currents were sensitive to 4AP at doses of 10 mM but not at the dose of 100 μM used in here[45]. Moreover, 4AP-sensitive potassium currents appear only after 3–4 weeks of neuronal differentiation in vitro[46]. This therefore suggests that 4AP influenced neurogenesis indirectly in cerebral spheroids through neurotransmitter release by mature neurons. To fully elucidate this mechanism, evaluating the effect of 4AP while blocking neurotransmitter release should be performed. Moreover, additional methods to induce increased neuronal activity, such as high extracellular potassium concentrations, and the inclusion of different glutamate receptor agonists, would help determine whether our observed changes in neurogenesis and miRNA expression are present in other hyperexcitable conditions as well as pinpoint the specific activity-dependent signaling pathway responsible for the phenomenon.

The mechanisms underlying 4AP -induced, activity associated neurogenesis remain unknown. Our data hints at the potential implication of miR-135a. This miRNA was shown to be important in exercise-induced neurogenesis in the mouse hippocampus where its downregulation was necessary for the formation of new neurons[47]. We found that the expression of miR-135a and its precursor pri-mir-135a2 is correlated with the expression of RMST. As the *MIR135A2* gene is located in the last intron of *RMST*, this would suggest a common promoter. RMST was shown to interact with SOX2 and its binding to the promoters of neurogenic genes, inducing neuronal differentiation of embryonic cells[48]. However, in this study, suppressing *RMST* expression did not decrease the expression of miR-135a2. It is possible that the RMST transcript is quickly spliced and pri-miR-135a2 rapidly generated after transcription. Therefore, the RMST mRNA is more abundant after splicing and preferentially targeted by siRNA. If this is the case, siRNA-mediated knock down of RMST would not be expected to significantly affect miR-135a levels. *RMST* expression is repressed by REST which has been shown to inhibit the expression of several neuronal genes and prevent neuronal differentiation[48,49]. It is unknown whether the decrease in *RMST* expression in our study is due to increased REST binding or not. Moreover, *RMST* transcription is at least partly under the control of the transcription factor Lmx1b and activated during Wnt signalling, which promotes neurogenesis. It has been shown that miR-135a2 in turn targets the transcripts of several Wnt pathway effectors, thereby acting as a negative feedback regulator to constrain neurogenesis[32]. Overall, a decrease in miR-135a expression may represent a permissive event for activity-induced neurogenesis and several other yet to be identified factors are likely to play additional roles.

Another question that remains unanswered is whether the decrease in miR-135a expression occurs specifically in NSCs or in other cell types, which then indirectly influence neuronal differentiation of NSCs. It has been shown that astrocytes can express miR-135a which participates in neuronal survival[50]. Evaluating the expression of miR-135a in individual cell types using fluorescent in situ hybridization or cell-sorting prior to RT-qPCR would be necessary to specifically address that question.

In conclusion, we have examined effects of 4AP on cerebral spheroids. 4AP enhanced neuronal differentiation and decreased glial differentiation of neural progenitors in this model. This is the first evidence of 4AP-induced activity dependent neurogenesis in human cerebral spheroids. We identified miR-135a as one potential mediator of activity-induced neurogenesis in this model, although the mechanisms underlying its function in this capacity remain undetermined.

Experimental procedures

Ethics guideline statement and informed consent statement.

Human iPSCs were obtained with informed written consent from healthy adult control subjects at the Massachusetts General Hospital (MGH), Department of Psychiatry and the study protocol was approved by the Institutional Review Board of the Massachusetts General Hospital in accordance with U.S. Common Rule ethical guidelines.

Use of the patient-derived iPSC lines and generation of cerebral organoids was performed with informed written consent at the University of Guelph and was approved by the University of Guelph Research Ethics Board (REB 17–11–012).

All methods were carried out in accordance with relevant guidelines and regulations.

Cerebral spheroid generation.

Human iPSCs were generated from neurologically normal individuals as described previously[51]. Briefly, iPSCs were generated from dermal skin punch (3 mm^3)-derived fibroblasts from healthy adult control subjects and reprogrammed as iPSCs using a nonintegrative, mRNA-based technology (Cellular Reprogramming, Inc. (www.cellular-reprogramming.com)). Human iPSCs were cultured in Essential 8 medium (ThermoFisher, Waltham, MA USA) or Nutristem hPSC XF medium (Biological Industries, Kibbutz Beit-Haemek, Israel) plated on Matrigel (Corning, Glendale, AZ USA) or Laminin-521 (Stemcell technologies, Vancouver, BC Canada) depending on the cell line. Cortical spheroids were generated from iPSCs following a previously described protocol with slight modifications. iPSCs were dissociated into single cells using Accutase (Gibco ThermoFisher). Cells were resuspended in Essential 8 medium supplemented with Y26732 ROCK inhibitor (Selleckchem, Houston, TX USA) at 10 μM and 10,000 cells were added to each well of an ultra-low attachment, U-bottom 96-well plate (ThermoFisher) to reaggregate overnight. The next day (noted as D0), medium was changed for E6 (Stemcell technologies) supplemented with 10 μM SMAD inhibitor SB431542 (Tocris, Bristol UK) and 2.5 μM SMAD inhibitor Dorsomorphin (Sigma-Aldrich, St. Louis, MO USA). This medium was replaced every day for 5 days. On day 6, spheroids were transferred to an ultra-low attachment 6-well plate placed on an orbital shaker at 65 rpm and medium was changed to Neurobasal medium (Gibco ThermoFisher) supplemented with 2% B27 supplements (Gibco ThermoFisher), 1% Penicillin/Streptomycin 10000U/L (Gibco ThermoFisher) and 1% GlutaMax (Gibco ThermoFisher). Basic Fibroblast Growth Factor (bFGF; 20 ng/ml, Stemcell technologies) and Epidermal Growth Factor (EGF; 20 ng/ml, Stemcell technologies) were added from day 6 to day 25. Medium was changed every day until day 15 and then every other day until day 25. On day 25, bFGF and EGF were replaced with Brain-derived Neurotrophic Factor (BDNF; 20 ng/ml, Stemcell technologies) and Neurotrophin-3 (NT-3; 20 ng/ml, Stemcell technologies) and the culture medium was changed every 3–4 days. On day 43, BDNF and NT-3 supplementation was stopped, and medium was changed every 3–4 days until spheroids were collected (see supplemental Fig. 1). Three different iPSC lines were used from 3 different individuals.

Immunofluorescence.

At selected time points, spheroids were collected, fixed in 4% paraformaldehyde (PFA), dehydrated in a 30% sucrose solution and 20 μM cryosections were acquired with a cryostat. Sections were permeabilized and blocked with 1% Bovine Serum Albumin (BSA, Sigma-Aldrich) and 0.3% Triton-X (FisherScientific) in PBS for 1 h at room temperature before incubation with primary antibodies overnight followed by incubation with Alexa Fluor 488 or 594-conjugated secondary antibodies (Supplementary Table 1) for 2 h at room temperature. Cells were then counterstained with 4′,6-diamidino-2-phenylindole (DAPI). For Ki67 immunohistochemistry, a heat-mediated antigen retrieval step was performed by incubating the slide in a sodium citrate buffer (10 mM sodium citrate, 0.05% Tween-20, pH = 6) for 20 min in a water bath at 95 °C prior to primary antibody incubation. Z-stacks were acquired on a FV1000 Olympus confocal microscope running Olympus Fluoview software version 4.3 (www.olympus-lifescience.com, Olympus, Tokyo, Japan). All stacks were acquired with the same settings between different biological replicates. Z-stacks and multi channel images were reconstructed using ImageJ (version 1.52e, Rasband, W.S., ImageJ, U. S. National Institutes of Health, Bethesda, Maryland, USA, https://imagej.nih.gov/ij/, 1997–2018). For cell quantification, 3 slices at least 40 μm apart were imaged with a 20X or 40X objective. Cells expressing each antigen were manually counted using ImageJ over the whole field of view and averaged between the 3 slices. The total number of cells to derive the proportion of each cell type was estimated by counting the numbers of DAPI stained nuclei using the Analyze Particle ImageJ plugin. Negative controls were performed by omitting the primary antibodies to control for non-specific binding of the secondary antibodies.

EdU labelling.

The EdU staining proliferation kit was used according to manufacturer's recommendations (Abcam). Briefly, spheroids were incubated with 20 μM EdU for 2 h before being exposed to 4AP for 8 h or vehicle (distilled water). Medium was changed to remove 4AP or vehicle. Two weeks later, spheroids were fixed, dehydrated and cryosectioned. Sections were then permeabilized and EdU was tagged using the fluorescent azide i647 before being incubated with primary and secondary antibodies as described above. Images were acquired and processed as described above.

Electrophysiology.

For whole-cell recording, spheroids were collected at selected time points and embedded in 3% Agarose. Embedded organoids were then cut in 400 μm thick slices with a Leica VT 1200 vibrating microtome (Leica Biosystems, Concord, Ontario, Canada) and slices were transferred into artificial cerebrospinal fluid (aCSF:128 mM NaCl, 10 mM D-glucose, 26 mM NaHCO$_3$, 2 mM CaCl$_2$, 2 mM MgSO$_4$, 3 mM KCl, 1.25 mM NaH$_2$PO$_4$, pH = 7.4) bubbled with 95% O$_2$ and 5% CO$_2$ at 30 °C for 1 h to recover. Slices were then transferred to a recording chamber (Warner Instruments, Hamden, CT USA) mounted on the stage of an Axioskop FS2 Microscope (Carl Zeiss Canada, Toronto, Ontario, Canada). Slices were superfused continuously with

aCSF bubbled with 95% O_2 and 5% CO_2 at room temperature. Spheroids smaller than 2 mm were not sliced and recorded as intact spheroids. Whole-cell recordings of putative neurons were performed with borosilicate glass pipette electrodes filled with an internal solution containing 120 mM K-gluconate, 5 mM KCl, 2 mM $MgCl_2$, 4 mM K_2-ATP, 400 µM Na_2-GTP, 10 mM Na_2-phosphocreatine and 10 mM HEPES buffer (adjusted to pH 7.3 with KOH). Pipette resistance was 4–6 MΩ. Whole-cell recordings were acquired at 20 kHz and lowpass filtered at 2 kHz using a Multiclamp 700B amplifier and Digidata 1440A digitizer (Molecular Devices, San Jose, CA, USA). Neuronal intrinsic excitability (input/output curve, rheobase) was assessed in current clamp mode by injecting positive current steps for 500 ms each. The frequency of spontaneous action potentials was measured in current clamp mode at resting membrane potential. The frequency and amplitude of spontaneous excitatory post-synaptic currents (sEPSCs) were recorded in voltage clamp mode with cells held at − 75 mV.

For multielectrode array (MEA) recordings, a single whole spheroid was transferred 2 h prior to recording into a well of a 6-well MEA with 64 low-impedance platinum microelectrodes (Axion Biosystems, Atlanta, GA USA) previously coated with 100 µg/ml poly-d-lysine (Sigma-Aldrich) and 10 µg/ml Laminin (Sigma-Aldrich). Before recording, culture medium was aspirated so that a minimal amount of medium (approximately 200 µL) covered the spheroid to minimize detachment and movement of spheroids. Recordings were performed on a Maestro Edge 384 channel system (Axion Biosystems, www.axionbiosystems.com) and AxIS software Spontaneous Neural Configuration v.2.0.4 (Axion Biosystems). Recordings were performed in culture medium at 37 °C with 5% CO_2 for 10 min. Baseline recordings were obtained after which spheroids were incubated with 4AP (Sigma-Aldrich) at 100 µM. This dose of 4AP was chosen based on previous publications and because it does not block potassium currents in neural stem cells[25–27,45]. Recordings were repeated 10 min and 1 h after addition of 4AP. Each recording sessions lasted 10 min. Analysis of the MEA recordings was performed with the Axion Biosystems Neural Metrics Tool using MATLAB scripts (version R2021a). Spikes were detected using an adaptative threshold of 5.5 times the standard deviation of the estimated noise for each electrode. Electrode bursts were defined as a minimum of 5 spikes with a maximum inter-spike interval of 100 ms. A network burst was defined as a minimum of 10 spikes under a maximum inter-spike interval of 100 ms with a minimum of 20% active electrodes[19].

Calcium imaging. Whole organoids were incubated for 30 min in culture medium with 2 µM of Fluo4-AM. Organoids were then washed and imaged on a FV1000 Olympus confocal microscope running Olympus Fluoview software version 4.3 (Olympus, Tokyo, Japan) using a 488 nm excitation laser. Images were acquired every 0.5 s for 3 min. After acquiring baseline recordings, organoids were stimulated with 100 µM of 4AP and recordings were repeated 10 min after exposure. The fluorescence of individual neurons was followed over time by manually drawing a region-of-interest (ROI) around each neuron and measuring the mean ROI fluorescence for each frame using ImageJ. Background fluorescence was subtracted from each measure and the relative change in fluorescence of each neuron was expressed as $(F-F_0)/F_0$ where F represents the mean fluorescence of a neuron at a particular time and F_0 represents the minimum fluorescence of that neuron. Calcium peaks were identified using custom Python scripts (version 3.8, Python Software Foundation, http://www.python.org) to identify local maxima. Only peaks with a prominence of 0.3 (representing an increase of 30% in fluorescence compared to the nearest local minima) were kept, discarding peaks due to noise only. Traces were visually inspected to confirm automatic peak detection. The calcium peak frequency, number of calcium peaks per cell and the number of cells showing at least one peak (active cells) were counted. The mean amplitude and duration of calcium transients for each active cell was also recorded.

RT-qPCR. Total RNA of individual spheroids was isolated with the miRNeasy micro Kit (Qiagen, Hilden, Germany) according to manufacturer's instructions. An on-column DNase digestion was performed with the RNase-free DNase set (Qiagen). RNA was quantified with the Nanodrop 2000c (ThermoFisher). For both mRNA and miRNA, 500 µg of total RNA was reverse transcribed. Messenger RNAs were reverse transcribed with qScript complementary DNA (cDNA) SuperMix (Quantabio, Berverly, MA USA). MicroRNAs were first polyadenylated and then reverse transcribed using the qScript miRNA cDNA Synthesis kit (Quantabio). Real-Time quantitative Polymerase Chain Reaction (RT-qPCR) was performed using a CFX96 Touch Real-Time PCR Detection System (Bio-Rad Laboratories) using 3 ng of cDNA per reaction and Sensifast SYBR No-ROX mix (Bioline Corporation, Alvinston, ON, Canada). Complementary DNA of mRNA was amplified using a pair of specific forward and reverse primers (Supplementary Table 2). MicroRNAs were amplified using a specific forward primer and PerfeCTa Universal PCR primer (Quantabio). Standard curves were performed for each primer pair to calculate primer efficiency. Primer specificity was assessed by performing a melting curve, examining the melting curve for multiple peaks, and separating the PCR products on a 1% Agarose gel and assessing the products for multiple bands. The stability of reference gene expression was evaluated using the GeNorm method[52]. GAPDH and HPRT were utilized as references for mRNA targets while miR-17 and miR-181c were utilized for miRNA normalization.

MicroRNA target functional annotation enrichment analysis. Validated mRNA targets of differentially expressed miRNAs were retrieved from the databases miRecords, miRTarbase v8 and Tarbase v8[53–55]. Enrichment for specific biological processes, molecular function and cellular compartment GO terms, as well as KEGG pathways, were analyzed with the ToppFunn module of the ToppGene suite using a probability density function with Benjamini–Hochberg False Discovery Rate (FDR) correction[56].

Statistics. Graphing and statistical analyses were performed with GraphPad Prism 7 (GraphPad Software, La Jolla, CA USA, www.graphpad.com/scientific-software/prism). Normal distribution of data was verified with

a Shapiro Wilk Test. If the data was normally distributed, differences between means were analyzed by Student's two-tailed *t* test or One-way ANOVA followed by multiple Student's *t* test with Holm Sidak's correction for multiple comparisons when there were more than 2 groups. If the data was not normally distributed, a Wilcoxon Rank Sum test was performed. For proportions, a logit-transformation was performed and Student's *t* tests were used on the logit transformed-data. Gene expression data from RT-qPCR was calculated using the $\Delta\Delta C_T$ method using qbase + software, version 3.2 (Biogazelle, Zwijnaarde, Belgium—www.qbaseplus.com) and $\log_2$ transformed to assume a normal distribution[57]. Correlations between gene expression were performed using a Pearson correlation. The number and nature of replicates is indicated in each figure. A *p*-value < 0.05 was considered statistically significant. Data shown represent the mean ± standard error of the mean (SEM). No prior sample size calculation was performed.

Data availability
RT-qPCR data is available in Supplementary file S2. Code for calcium imaging is available at https://github.com/Thomas-Parmentier/calcium-imaging-cultured-cells.

References

1. Deng, W., Aimone, J. B. & Gage, F. H. New neurons and new memories: How does adult hippocampal neurogenesis affect learning and memory?. *Nat. Rev. Neurosci.* **11**, 339–350 (2010).
2. Moreno-Jiménez, E. P. *et al.* Adult hippocampal neurogenesis is abundant in neurologically healthy subjects and drops sharply in patients with Alzheimer's disease. *Nat. Med.* **25**, 554–560 (2019).
3. Tashiro, A., Makino, H. & Gage, F. H. Experience-specific functional modification of the dentate gyrus through adult neurogenesis: A critical period during an immature stage. *J. Neurosci.* **27**, 3252–3259 (2007).
4. Bruel-Jungerman, E., Davis, S., Rampon, C. & Laroche, S. Long-term potentiation enhances neurogenesis in the adult dentate gyrus. *J. Neurosci.* **26**, 5888–5893 (2006).
5. Gould, E., Beylin, A., Tanapat, P., Reeves, A. & Shors, T. J. Learning enhances adult neurogenesis in the hippocampal formation. *Nat. Neurosci.* **2**, 260–265 (1999).
6. van Praag, H. Exercise enhances learning and hippocampal neurogenesis in aged mice. *J. Neurosci.* **25**, 8680–8685 (2005).
7. Jessberger, S. *et al.* Seizure-associated, aberrant neurogenesis in adult rats characterized with retrovirus-mediated cell labeling. *J. Neurosci.* **27**, 9400–9407 (2007).
8. Bao, H. *et al.* Long-range gabaergic inputs regulate neural stem cell quiescence and control adult hippocampal neurogenesis. *Cell Stem Cell* **21**, 604-617.e5 (2017).
9. Botterill, J. J., Brymer, K. J., Caruncho, H. J. & Kalynchuk, L. E. Aberrant hippocampal neurogenesis after limbic kindling: Relationship to BDNF and hippocampal-dependent memory. *Epilepsy Behav.* **47**, 83–92 (2015).
10. Deisseroth, K. *et al.* Excitation-neurogenesis coupling in adult neural stem/progenitor cells. *Neuron* **42**, 535–552 (2004).
11. Tozuka, Y., Fukuda, S., Namba, T., Seki, T. & Hisatsune, T. GABAergic excitation promotes neuronal differentiation in adult hippocampal progenitor cells. *Neuron* **47**, 803–815 (2005).
12. Eiraku, M. *et al.* Self-organized formation of polarized cortical tissues from ESCS and its active manipulation by extrinsic signals. *Cell Stem Cell* **3**, 519–532 (2008).
13. Gordon, A. *et al.* Long-term maturation of human cortical organoids matches key early postnatal transitions. *Nat. Neurosci.* **24**, 331–342 (2021).
14. Lancaster, M. A. & Knoblich, J. A. Generation of cerebral organoids from human pluripotent stem cells. *Nat. Protoc.* **9**, 2329–2340 (2014).
15. Paşca, A. M. *et al.* Functional cortical neurons and astrocytes from human pluripotent stem cells in 3D culture. *Nat. Methods* **12**, 671–678 (2015).
16. Quadrato, G. *et al.* Cell diversity and network dynamics in photosensitive human brain organoids. *Nature* **545**, 48–53 (2017).
17. Tanaka, Y., Cakir, B., Xiang, Y., Sullivan, G. J. & Park, I.-H. Synthetic analyses of single-cell transcriptomes from multiple brain organoids and fetal brain. *Cell Rep.* **30**, 1682-1689.e3 (2020).
18. Velasco, S. *et al.* Individual brain organoids reproducibly form cell diversity of the human cerebral cortex. *Nature* **570**, 523–527 (2019).
19. Trujillo, C. A. *et al.* Complex oscillatory waves emerging from cortical organoids model early human brain network development. *Cell Stem Cell* https://doi.org/10.1016/j.stem.2019.08.002 (2019).
20. Birey, F. *et al.* Assembly of functionally integrated human forebrain spheroids. *Nature* **545**, 54–59 (2017).
21. Sun, A. X. *et al.* Potassium channel dysfunction in human neuronal models of Angelman syndrome. *Science* **366**, 1486–1492 (2019).
22. Trujillo, C. A. *et al.* Pharmacological reversal of synaptic and network pathology in human MECP2-KO neurons and cortical organoids. *EMBO Mol. Med.* **13**, e12523 (2021).
23. Yoon, S.-J. *et al.* Reliability of human cortical organoid generation. *Nat. Methods* **16**, 75–78 (2019).
24. Sloan, S. A., Andersen, J., Paşca, A. M., Birey, F. & Paşca, S. P. Generation and assembly of human brain region–specific three-dimensional cultures. *Nat. Protoc.* **13**, 2062–2085 (2018).
25. Gonzalez-Sulser, A. *et al.* The 4-aminopyridine in vitro epilepsy model analyzed with a perforated multi-electrode array. *Neuropharmacology* **60**, 1142–1153 (2011).
26. Heuzeroth, H., Wawra, M., Fidzinski, P., Dag, R. & Holtkamp, M. The 4-aminopyridine model of acute seizures in vitro elucidates efficacy of new antiepileptic drugs. *Front. Neurosci.* **13**, 2 (2019).
27. Hsiao, M.-C. *et al.* An in vitro seizure model from human hippocampal slices using multi-electrode arrays. *J. Neurosci. Methods* **244**, 154–163 (2015).
28. Olde Loohuis, N. F. M. *et al.* MicroRNA networks direct neuronal development and plasticity. *Cell. Mol. Life Sci.* **69**, 89–102 (2012).
29. Shen, Q. & Temple, S. Fine control: MicroRNA regulation of adult neurogenesis. *Nat. Neurosci.* **12**, 369 (2009).
30. Eacker, S. M., Keuss, M. J., Berezikov, E., Dawson, V. L. & Dawson, T. M. Neuronal activity regulates hippocampal miRNA expression. *PLoS ONE* **6**, e25068 (2011).
31. Korotkov, A., Mills, J. D., Gorter, J. A., van Vliet, E. A. & Aronica, E. Systematic review and meta-analysis of differentially expressed miRNAs in experimental and human temporal lobe epilepsy. *Sci. Rep.* **7**, 11592 (2017).
32. Anderegg, A. & Awatramani, R. Making a mes: A transcription factor-microRNA pair governs the size of the midbrain and the dopaminergic progenitor pool. *Neurogenesis* **2**, e998101 (2015).
33. Lancaster, M. A. *et al.* Cerebral organoids model human brain development and microcephaly. *Nature* **501**, 373–379 (2013).

34. Tyssowski, K. M. *et al.* Different neuronal activity patterns induce different gene expression programs. *Neuron* **98**, 530-546.e11 (2018).
35. Sakaguchi, H. *et al.* Self-organized synchronous calcium transients in a cultured human neural network derived from cerebral organoids. *Stem Cell Rep.* **13**, 458–473 (2019).
36. Yin, J. & VanDongen, A. M. Enhanced neuronal activity and asynchronous calcium transients revealed in a 3D organoid model of Alzheimer's disease. *ACS Biomater. Sci. Eng.* **7**, 254–264 (2021).
37. Fair, S. R. *et al.* Electrophysiological maturation of cerebral organoids correlates with dynamic morphological and cellular development. *Stem Cell Rep.* **15**, 855–868 (2020).
38. Yokoi, R. *et al.* Analysis of signal components < 500 Hz in brain organoids coupled to microelectrode arrays: A reliable test-bed for preclinical seizure liability assessment of drugs and screening of antiepileptic drugs. *Biochem. Biophys. Rep.* **28**, 101148 (2021).
39. Giandomenico, S. L. *et al.* Cerebral organoids at the air–liquid interface generate diverse nerve tracts with functional output. *Nat. Neurosci.* **22**, 669–679 (2019).
40. Durens, M. *et al.* High-throughput screening of human induced pluripotent stem cell-derived brain organoids. *J. Neurosci. Methods* **335**, 108627 (2020).
41. Foliaki, S. T. *et al.* Neuronal excitatory-to-inhibitory balance is altered in cerebral organoid models of genetic neurological diseases. *Mol Brain* **14**, 156 (2021).
42. Ma, D. K., Kim, W. R., Ming, G. & Song, H. Activity-dependent extrinsic regulation of adult olfactory bulb and hippocampal neurogenesis. *Ann. N. Y. Acad. Sci.* **1170**, 664–673 (2009).
43. Song, J., Olsen, R. H. J., Sun, J., Ming, G. & Song, H. Neuronal circuitry mechanisms regulating adult mammalian neurogenesis. *Cold Spring Harb. Perspect. Biol.* **8**, a018937 (2016).
44. Avoli, M. & Jefferys, J. G. R. Models of drug-induced epileptiform synchronization in vitro. *J. Neurosci. Methods* **260**, 26–32 (2016).
45. Schaarschmidt, G., Wegner, F., Schwarz, S. C., Schmidt, H. & Schwarz, J. Characterization of voltage-gated potassium channels in human neural progenitor cells. *PLoS ONE* **4**, e6168 (2009).
46. Song, M., Mohamad, O., Chen, D. & Yu, S. P. Coordinated development of voltage-gated Na^+ and K^+ currents regulates functional maturation of forebrain neurons derived from human induced pluripotent stem cells. *Stem Cells Dev.* **22**, 1551–1563 (2013).
47. Pons-Espinal, M. *et al.* MiR-135a-5p is critical for exercise-induced adult neurogenesis. *Stem Cell Rep.* **12**, 1298–1312 (2019).
48. Ng, S.-Y., Bogu, G. K., Soh, B. S. & Stanton, L. W. The long noncoding RNA RMST interacts with SOX2 to regulate neurogenesis. *Mol. Cell* **51**, 349–359 (2013).
49. Conaco, C., Otto, S., Han, J.-J. & Mandel, G. Reciprocal actions of REST and a microRNA promote neuronal identity. *Proc. Natl. Acad. Sci.* **103**, 2422–2427 (2006).
50. Chu, Y.-Y. *et al.* Astrocytic CCAAT/enhancer binding protein δ regulates neuronal viability and spatial learning ability via miR-135a. *Mol. Neurobiol.* **53**, 4173–4188 (2016).
51. Zimmerman, A. J. *et al.* A psychiatric disease-related circular RNA controls synaptic gene expression and cognition. *Mol. Psychiatry* **25**, 2712–2727 (2020).
52. Vandesompele, J., Preter, K. D., Roy, N. V. & Paepe, A. D. Accurate normalization of real-time quantitative RT-PCR data by geometric averaging of multiple internal control genes. *Genome Biol.* **3**, 12 (2002).
53. Huang, H.-Y. *et al.* miRTarBase 2020: Updates to the experimentally validated microRNA–target interaction database. *Nucleic Acids Res.* https://doi.org/10.1093/nar/gkz896 (2019).
54. Sethupathy, P. TarBase: A comprehensive database of experimentally supported animal microRNA targets. *RNA* **12**, 192–197 (2005).
55. Xiao, F. *et al.* miRecords: an integrated resource for microRNA-target interactions. *Nucleic Acids Res.* **37**, D105–D110 (2009).
56. Chen, J., Bardes, E. E., Aronow, B. J. & Jegga, A. G. ToppGene suite for gene list enrichment analysis and candidate gene prioritization. *Nucleic Acids Res.* **37**, W305–W311 (2009).
57. Pfaffl, M. W. A new mathematical model for relative quantification in real-time RT-PCR. *Nucleic Acids Res.* **29**, 45e–445 (2001).

Acknowledgements

Author contributions

T.P. and J.LaM. designed the project. T.P., E.H. and N.W. performed all experiments. T.P. and J.LaM. analyzed the data. F.J., C.B., S.D.S., R.H.P., M.P., L.G., J.Lal., and J.LaM. provided resources, conceptualization, and intellectual content. T.P. and J. LaM. wrote the paper with feedback from all authors.

Competing interests

The authors declare no competing interests.

Additional information

Supplementary Information The online version contains supplementary material available at https://doi.org/10.1038/s41598-022-13071-x.

Correspondence and requests for materials should be addressed to J.L.

Reprints and permissions information is available at www.nature.com/reprints.

Publisher's note Springer Nature remains neutral with regard to jurisdictional claims in published maps and institutional affiliations.